Chemistry & Biology
Article

Stable Isotope-Labeled Raman Imaging Reveals Dynamic Proteome Localization to Lipid Droplets in Single Fission Yeast Cells

Hemanth Nag Noothalapati Venkata[1] and Shinsuke Shigeto[1,*]
[1]Department of Applied Chemistry and Institute of Molecular Science, National Chiao Tung University, Hsinchu 300, Taiwan
*Correspondence: shigeto@mail.nctu.edu.tw
http://dx.doi.org/10.1016/j.chembiol.2012.08.020

SUMMARY

Lipid droplets have been hypothesized to be intimately associated with intracellular proteins. However, there is little direct evidence for both spatiotemporal and functional relations between lipid droplets and proteins provided by molecular-level studies on intact cells. Here, we present in vivo time-lapse Raman imaging, coupled with stable-isotope (^{13}C) labeling, of single living *Schizosaccharomyces pombe* cells. Using characteristic Raman bands of proteins and lipids, we dynamically visualized the process by which ^{13}C-glucose in the medium was assimilated into those intracellular components. Our results show that the proteins newly synthesized from incorporated ^{13}C-substrate are localized specifically to lipid droplets as the lipid concentration within the cell increases. We demonstrate that the present method offers a unique platform for proteome visualization without the need for tagging individual proteins with fluorescent probes.

INTRODUCTION

Lipid droplets are globular organelles that are ubiquitously found in most eukaryotic cells from yeast to mammals. They were long considered as a static energy storage containing neutral lipids, such as triacylglycerols and sterol esters, and thus remained the least characterized cytoplasmic organelle. In the past half decade, however, lipid droplets have come under the spotlight of cell biology. There is now growing evidence that reveals diverse roles and an intrinsically dynamic nature of lipid droplets as a key player in various cellular processes, such as lipid homeostasis and cell signaling (Digel et al., 2010; Fujimoto and Ohsaki, 2006; Martin and Parton, 2006; Murphy et al., 2009; Thiele and Spandl, 2008; Walther and Farese, 2009). It has also been shown that lipid droplets are relevant to many serious health issues, including obesity, type 2 diabetes, and atherosclerosis. Among various functions of lipid droplets, a recently proposed hypothesis that lipid droplets serve to temporarily sequester proteins is thought provoking and might potentially deepen our understanding of lipid droplets (Cermelli et al., 2006; Hodges and Wu, 2010; Welte, 2007). Proteomic studies have detected lipid droplet-associated proteins in many cell types (Grillitsch et al., 2011; Hodges and Wu, 2010), which apparently have little to do with lipid metabolism. Those proteins include histones (Cermelli et al., 2006), caveolins (Pol et al., 2004), and perilipin family proteins (Brasaemle, 2007). Although proteomic analysis is very powerful for identifying and characterizing individual key proteins, biochemical fractionation and purification procedures adopted in lipid-droplet proteomics are vulnerable to contamination. Moreover, proteomic analysis cannot provide information on spatial localization (distribution) of proteins as well as their temporal evolution. To test whether lipid droplets are both spatiotemporally and functionally associated with proteins (e.g., sequestration), direct evidence needs to be obtained from single living cells using microscopic and imaging techniques.

Molecular imaging based on linear/nonlinear Raman spectroscopy has emerged as a promising tool to trace intracellular processes in vivo and at the molecular level. In contrast with commonly employed fluorescence microscopy, Raman-based methods require no exogenous probe to be introduced to cells. Vibrational resonances, which are an inherent property of molecules, give rise to chemical specificity and, hence, enable label-free molecular imaging. Of particular importance is work using coherent anti-Stokes Raman scattering (CARS) microscopy, which has high sensitivity and three-dimensional sectioning capability. The Xie group at Harvard demonstrated video-rate CARS imaging of living cells and tissues (Evans et al., 2005). Hellerer et al. (2007) also used CARS microscopy to visualize lipid distributions in *Caenorhabditis elegans*. Very recently, Xie and coworkers have further improved image contrast by using stimulated Raman scattering (SRS) instead of CARS (Freudiger et al., 2011; Saar et al., 2010). SRS is, in principle, free from the nonresonant background that always interferes with vibrationally resonant signals in CARS. These nonlinear Raman microscopic studies achieved to date mostly rely on the strong C-H stretch vibrations around 2850 cm^{-1} (Evans et al., 2005; Freudiger et al., 2011; Hellerer et al., 2007; Kano and Hamaguchi, 2007; Nan et al., 2003; Saar et al., 2010). However, C-H stretch images alone do not allow us to directly look into the interplay between lipid droplets and proteins and other organelles. In contrast, Raman microspectroscopy and imaging (Huang et al., 2005, 2012; Matthäus et al., 2006; Noothalapati Venkata et al., 2011; van Manen et al., 2005; Wu et al., 2011), although taking longer data acquisition time, provide more extensive and detailed molecular information than CARS microscopy without the need for complicated spectral analysis (Rinia et al., 2008; Vartiainen et al., 1990).

Here, we present time-lapse Raman microspectroscopy and imaging, coupled with stable-isotope labeling, of living fission yeast *Schizosaccharomyces pombe* cells. Stable-isotope probing (SIP), in which stable isotopes such as ^{13}C and ^{15}N are incorporated in cells as a nonperturbative tracer for RNA (Manefield et al., 2002), DNA (Radajewski et al., 2000), and proteins (Jehmlich et al., 2010), has been widely used for microbial identification. When combined with Raman imaging (Haider et al., 2010; Huang et al., 2007; Matthäus et al., 2008; van Manen et al., 2008), the stable-isotope labeling strategy can confer an ability to differentiate between cellular components produced through distinct anabolic pathways and temporal evolutions. This ability arises from the fact that the characteristic frequency of an oscillator representing a molecular vibration is inversely proportional to the square root of the reduced mass of the oscillator; the heavier the incorporated isotope, the lower the frequency (i.e., redshift in a Raman spectrum).

In the present study, we cultured *S. pombe* cells in minimal medium with ^{13}C-glucose as a primary carbon source and monitored subsequent ^{13}C incorporation into cellular components both in bulk experiments, where 25 cells were randomly picked up from bulk culture at different ^{13}C incubation times, and in single-cell imaging experiments, where a target *S. pombe* cell was continuously observed. In bulk experiments, we observed Raman spectral changes during the course of ^{13}C incorporation in *S. pombe* cells, from which we derived a holistic (but averaged) view of the incorporation dynamics and determined our marker bands for single-cell imaging. Among many Raman bands, we chose the ring breathing mode of phenylalanine (Phe) residues at 1003 cm^{-1} as a protein Raman marker. This band undergoes a large ^{13}C shift of 36 cm^{-1} (1003 → 967 cm^{-1}). Intriguingly, the results of single-cell imaging experiments revealed that proteins newly formed from incorporated ^{13}C (identified by the 967 cm^{-1} band) are localized to lipid droplets (identified by lipid Raman bands at 1301 and 1602 cm^{-1}) at a specific stage. This colocalization was unique to the ^{13}C-substituted proteins, because the distribution of unsubstituted proteins did not show any coincidence with that of the lipid droplets. Moreover, we found that the colocalization phenomenon occurs irrespective of growth phases and strains of *S. pombe*. Although global analysis of protein localization (~90% of the proteome) in fission yeast was already reported (Matsuyama et al., 2006), the localization to lipid droplets has been uncovered for the first time, to our knowledge, in this work. The present findings strongly corroborate on a single-cell basis the hypothesis that proteins associated with lipid metabolism are synthesized on site or recruited specifically to lipid droplets (Welte, 2007), possibly induced by starvation.

RESULTS AND DISCUSSION

Yeast Shows Similar Growth Curves in ^{12}C- and ^{13}C-Media

S. pombe cells cultured in ^{12}C- and ^{13}C-glucose containing Edinburgh Minimal Medium (EMM; see the Experimental Procedures) broth showed quite a similar growth characteristics, confirming that cells grown in ^{13}C-EMM perform normal metabolic activities.

Bulk Experiments Provide an Overview of ^{13}C Incorporation Process

Space- and time-resolved Raman measurements provide a holistic view of ^{13}C incorporation in *S. pombe* cells from bulk culture. We recorded a series of Raman spectra at two different intracellular locations—namely, the cytoplasm (Figure 1A) and lipid droplets (Figure 1B)—at 0, 3.5, 8, 15, 23, 31, and 40 hr after inoculation in ^{13}C-EMM. Each spectrum is an average of 25 spectra obtained from 25 randomly selected *S. pombe* cells. The cytoplasm is usually rich in proteins, so the 0 hr spectrum of Figure 1A is dominated by protein Raman bands of *S. pombe* cultured in ordinary unsubstituted medium. Prominent Raman features include the amide I band at 1654 cm^{-1}, the C-H bending mode of the aliphatic chain at 1451 and 1338 cm^{-1}, and the phenylalanine ring breathing mode at 1003 cm^{-1}. As ^{13}C incubation time is prolonged, the intensity of the amide I band at 1654 cm^{-1} decreases and the corresponding ^{13}C-substituted band emerges at 1620 cm^{-1} (34 cm^{-1} isotope shift). Likewise, the phenylalanine band at 1003 cm^{-1} disappears concomitantly with the growth of a new band at 967 cm^{-1} (36 cm^{-1} isotope shift). In contrast, the 1451 and 1338 cm^{-1} bands remain unshifted. The observed ^{13}C-substitution effects agree well with previous reports (Haider et al., 2010; Huang et al., 2007; Onogi et al., 2009).

The averaged spectrum of lipid-rich regions at 0 hr (Figure 1B) primarily contains lipid Raman bands (Huang et al., 2005; Naumann, 2001): 1654 cm^{-1} (*cis*-C = C stretch), 1602 cm^{-1} (assigned at least partially to the C = C stretch of ergosterol; Chiu et al., 2012), 1440 cm^{-1} (CH bend), and 1301 cm^{-1} (in-plane CH_2 twist). With increasing ^{13}C-glucose culturing time, the 1654 cm^{-1} band disappears and the corresponding ^{13}C-substituted band appears at 1595 cm^{-1}, slightly below 1602 cm^{-1}. The shift of 59 cm^{-1} (1654 → 1595 cm^{-1}) is almost exactly what is expected from the $^{13}C/^{12}C$ mass ratio: $1654 \times (12/13)^{1/2} \approx 1589$. The 1602 cm^{-1} band in turn moves to 1542 cm^{-1}, but the region around 1600 cm^{-1} is never cleared up because of the arising band at 1595 cm^{-1}. Similar to the case of the cytoplasmic spectra (Figure 1A), the bands at 1440 and 1301 cm^{-1} exhibit no apparent isotope effect. Again, the observed trend in frequency shift is consistent with the literature (Haider et al., 2010; Huang et al., 2007; Onogi et al., 2009). The assignments and observed isotope shifts of the Raman bands discussed above are summarized as Table 1.

To examine how well the averaged spectra in Figures 1A and 1B represent individual spectra recorded in 25 cells, we computed Pearson correlation coefficients for the whole spectral window (300–1800 cm^{-1}) at each ^{13}C incubation time. As shown in Figure 1C for the cytoplasm and Figure 1D for lipid droplets, the correlation coefficients obtained are very large (>90% similarity). This result ensures that the averaged spectra are indeed representative of 25 individual spectra. Note that the similarity decreases by a maximum of 8% at intermediate incubation times (i.e., 8, 15, and 23 hr), indicating that there was a relatively larger variation at these times in the degree of ^{13}C incorporation among 25 cells studied than at 0 hr (no ^{13}C substitution in all cells) and 40 hr (complete ^{13}C substitution in virtually all cells).

The time-stream of averaged Raman spectra shown in Figures 1A and 1B also provides quantitative insight into the ^{13}C incorporation dynamics. Figure 2 plots the area intensities (see the

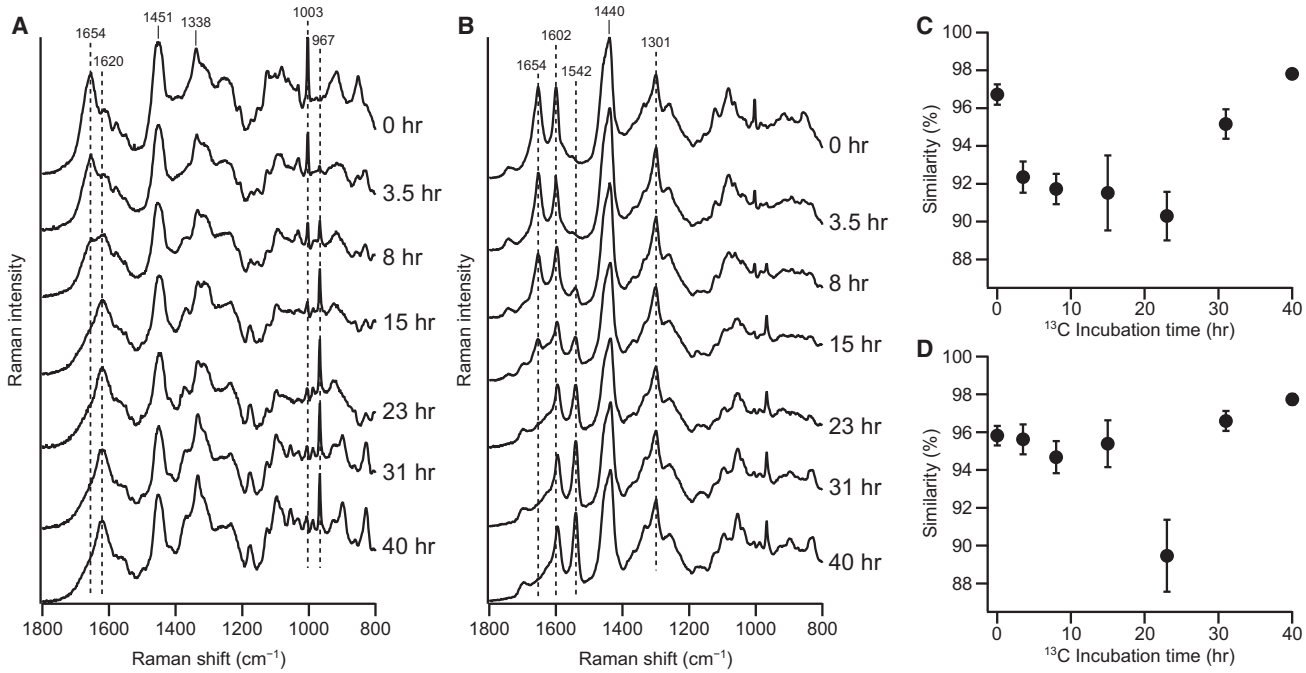

Figure 1. Space-Resolved Raman Measurements on Randomly Selected *S. pombe* Cells at Different ^{13}C Incubation Times

(A and B) Average of 25 Raman spectra measured in the cytoplasm (A) and in lipid droplets (B), at 0, 3.5, 8, 15, 23, 31, and 40 hr after inoculation in ^{13}C-EMM. (C and D) Pearson correlation coefficients calculated for the whole region (300–1800 cm^{-1}) of the protein-rich (C) and lipid-rich (D) Raman spectra at each ^{13}C incubation time. Data represent mean values ± standard deviations; n = 25.

Experimental Procedures) of three representative pairs of Raman bands versus ^{13}C incubation time. The intensities of the 1654 cm^{-1} band (Figure 2A, open circle) and the 1003 cm^{-1} band (Figure 2B, open circle) both decay at nearly the same rate within 15 hr. Along with this decay, the ^{13}C-substituted counterparts at 1620 cm^{-1} (Figure 2A, closed circle) and 967 cm^{-1} (Figure 2B, closed circle) rise at a slightly slower rate and reach a plateau after one day. Note that the intensity of the 1003 cm^{-1} band does not fall to zero even after 15 hr because of a very weak band that either is originally present at the same wave number or emerges as a result of ^{13}C substitution of an unidentified band. We conclude from Figures 2A and 2B that a complete depletion of the ^{12}C content takes about 15 hr, whereas complete ^{13}C incorporation in cytoplasmic proteins requires about 24 hr. Because doubling time of fission yeast in EMM broth is generally in between 2 and 4 hr, the time required for ^{13}C-glucose to be assimilated in proteins is estimated to be 10 generations, reflecting active protein synthesis. In contrast, ^{13}C-isotope substitution in lipids takes longer than in proteins. The intensity of the $^{12}C = {}^{12}C$ stretch band at 1654 cm^{-1} observed in lipid-rich regions (Figure 2C, open circle) decreases at an obviously slower rate than that of the amide I (^{12}C) band does (Figure 2A, open circle) and is entirely depleted only at 23 hr. The slower incorporation dynamics associated with lipids is also evident from the rise of the 1542 cm^{-1} band (Figure 2C, closed circle). Here, we made an indirect comparison of the time profile of the 1654 cm^{-1} band with that of the 1542 cm^{-1} band, instead of the 1595 cm^{-1} band, because the appearance of the $^{13}C = {}^{13}C$ stretch band at 1595 cm^{-1} is interfered with the 1602 cm^{-1} band.

Single-Cell Imaging Reveals Localization of Proteins to Lipid Droplets

We now have gained a detailed picture of how Raman spectra of the cytoplasm and lipid droplets vary as ^{13}C-glucose is assimilated in *S. pombe* cells. However, those data were obtained by averaging behaviors of many different *S. pombe* cells, so they do not provide information on spatial distributions of the cellular components within a single cell and their temporal changes during the course of ^{13}C incorporation. To address these crucial issues, we need to combine the ^{13}C labeling with time-lapse Raman imaging on a single *S. pombe* cell. Here, we use the Phe band (at 1003 cm^{-1} for ^{12}C and 967 cm^{-1} for ^{13}C) to generate protein Raman images for the following reasons: First, it is a very sharp, easily discernible band that is located in a relatively less congested region of the spectrum. Second, the band exhibits a pronounced ^{13}C shift of 36 cm^{-1} from 1003 to 967 cm^{-1} (see Figures 1A and 1B). Third, unlike other Raman bands of amino acid residues (e.g., tyrosine doublet at 825 and 853 cm^{-1}; Siamwiza et al., 1975), the intensity of the Phe band is insensitive to the surrounding environment of the protein (Li et al., 1990). Therefore, the Phe band solely reflects the concentration of the moiety. Last, phenylalanine residues are usually abundant in proteins, so the 1003 cm^{-1} band can probe nearly the whole intracellular population of proteins at a given instant. In other words, this Raman band manifests the proteome. For markers of lipid droplets, we use the bands at 1301 and 1602 cm^{-1}.

Figure 3 shows time-lapse Raman images over 37 hr, constructed at 1003, 967, 1301, and 1602 cm^{-1}, of a single stationary-phase *S. pombe* cell with green fluorescence protein

Table 1. Assignments of and ^{13}C-Isotope Effects on the Representative Raman Bands of Proteins and Lipids

Frequency in ^{12}C Medium (cm^{-1})	Frequency in ^{13}C Medium (cm^{-1})	^{13}C Shift (cm^{-1})	Assignment
1,654	1,620	34	Amide I mode (protein)
1,654	1,595	59	*cis*-C = C stretch (lipid)
1,602	1,542	60	C = C stretch (mainly ergosterol)
1,440	1,440	0	CH bend (both protein and lipid)
1,301	1,301	0	In-plane CH_2 twist (lipid)
1,003	967	36	Ring breathing mode of phenylalanine residues (protein)

(GFP)-labeled mitochondria fed with ^{13}C-glucose. All the four Raman images at a given measurement time were obtained simultaneously from one two-dimensional scan of the cell. Each Raman image is represented in a pseudocolor scale (red, magenta, cyan, yellow, or rainbow). For example, a red pseudocolor scale in which the highest intensities appear white, the moderate appear red, and the lowest appear black is used for the Raman images at 1003 cm^{-1} (Figure 3C). Because the intensity of a Raman band is proportional to the concentration of the molecular species that gives rise to the Raman band, the Raman image of that band displays a concentration map for the species. Also shown in Figure 3 are bright-field optical micrographs (Figure 3A) and GFP fluorescence images (Figure 3B) of the *S. pombe* cell. The optical micrographs are silent about molecular distribution, although lipid droplets of ~0.1 μm size can be seen as black dots (as indicated by arrows at 31 hr). The GFP image clearly visualizes mitochondrial distribution at each time.

Let us examine first a pair of the time-lapse Raman images of the Phe band for proteins. The Raman images at 1003 cm^{-1} (Figure 3C) represent the distribution of Phe-containing proteins that are originally present within the *S. pombe* cell when we started the imaging experiment, whereas those at 967 cm^{-1} (Figure 3D) map the distribution of newly formed proteins using exogenous ^{13}C substrate. One hour after inoculation in ^{13}C-EMM, proteins are distributed homogenously across the cell and ^{13}C is not yet incorporated into proteins. As time progresses, the ^{12}C content in proteins is depleted particularly in two regions where many lipid droplets are seen. After 31 hr, the intensity of the 1003 cm^{-1} band decreases to a noise level. Protein synthesis machinery, which is known to be continuously operating, utilizes ^{13}C substrate taken up in the cell to fulfill its mission. As a result, the concentration of ^{13}C-labeled proteins probed at 967 cm^{-1} gradually increases (Figure 3D), which is consistent with the results of the bulk experiments. In sharp contrast with the existing ^{12}C proteins, newly formed ^{13}C-labeled proteins show a heterogeneous distribution pattern (see the images at 25 and 31 hr), and more importantly, are localized to the region where lipids are highly concentrated—that is, lipid droplets. At 37 hr, the distribution of ^{13}C-labeled proteins becomes homogeneous again.

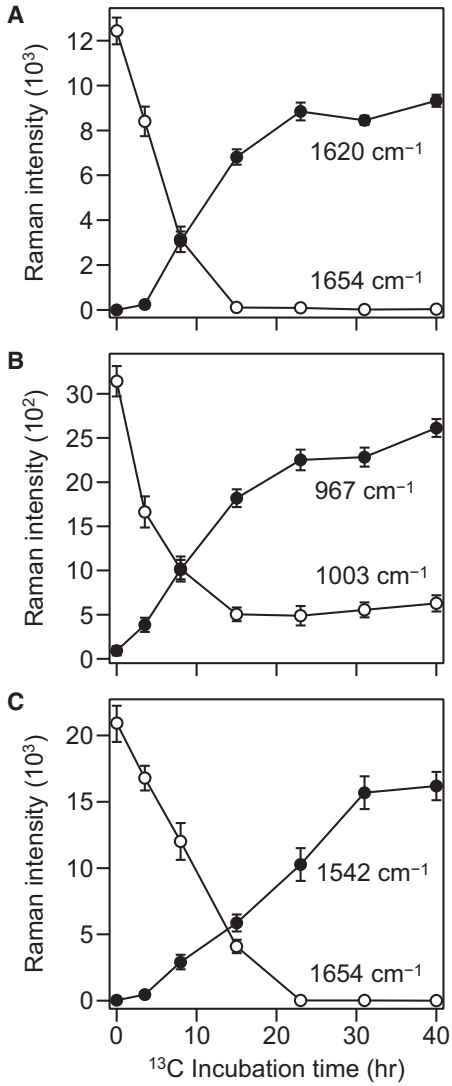

Figure 2. ^{13}C Incorporation Dynamics Observed in the Bulk Experiments

(A) Amide I bands in the cytoplasmic spectrum at 1654 cm^{-1} (open circle) and 1620 cm^{-1} (closed circle). The amide I mode is predominantly assigned to the C = O stretch of the peptide bond of proteins. Upon ^{13}C substitution, the amide I vibrational frequency shifts from 1654 to 1620 cm^{-1}.

(B) Phenylalanine ring-breathing mode in the cytoplasmic spectrum at 1003 cm^{-1} (open circle) and 967 cm^{-1} (closed circle). Upon ^{13}C substitution, the Phe breathing frequency shifts from 1003 to 967 cm^{-1}.

(C) ^{12}C = ^{12}C stretch band at 1654 cm^{-1} (open circle) and the ^{13}C-shifted 1602 cm^{-1} band (closed circle) in the lipid droplet spectrum.

Data represent mean values ± standard deviations; n = 25.

We next look into the Raman images of lipids at 1301 cm^{-1} (Figure 3E). Lipids are localized near two ends of the cell (Huang et al., 2011) at all measurement times except for 37 hr, at which the distribution appears to be more uniform. In addition, the total concentration of lipids increases after 15 hr. The Raman images at 1602 cm^{-1} (Figure 3F) markedly resemble those at 1301 cm^{-1}. This resemblance is not surprising because the 1602 cm^{-1} band is associated with ergosterol (Chiu et al., 2012), which is a fragment of sterol esters, a major constituent of the lipid-droplet

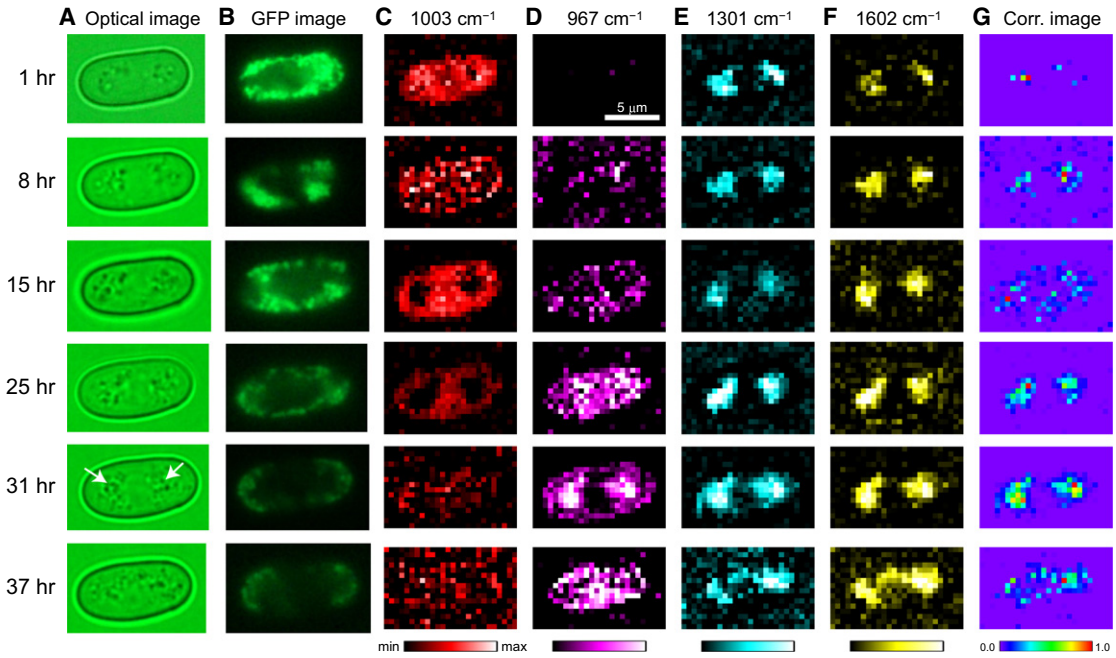

Figure 3. Time-Lapse Multimode Raman Imaging of a Single Living *S. pombe* Cell Grown in ^{13}C-Glucose-Containing Medium

(A) Bright-field optical images of the target cell. Arrows at 31 hr indicate the regions where there are many lipid droplets. Lipid droplets are identified as black dots.

(B) GFP fluorescence images of mitochondria of the cell.

(C–F) Raman images constructed at 1003 (Phe breathing mode of ^{12}C-proteins), 967 (Phe breathing mode of ^{13}C-substituted proteins), 1301 (in-plane CH_2 twist of lipids), and 1602 cm^{-1}. The scale bar in (D) measures 5 μm and also applies to the other images.

(G) Correlation images between D and E. The correlation coefficient at each pixel was computed using the equation given in the text.

core. According to our bulk experiments (see above), the 1301 cm^{-1} band shows no ^{13}C shift, whereas the 1602 cm^{-1} band shows a 60 cm^{-1} shift. In the imaging experiment, however, the total intensity of the 1602 cm^{-1} band within the *S. pombe* cell does not decrease at all with time. This result suggests that a majority of lipids are synthesized by consuming ^{12}C substrate available within the cell.

We have assigned above the lipid-rich regions in the cell predominantly to lipid droplets. This assignment is supported by the following pieces of evidence. First, in yeast, mitochondria, along with lipid droplets, are known to be the major organelle where lipids are abundant, so the Raman images shown in Figure 3E could be associated with mitochondria rather than with lipid droplets. However, the GFP-labeled mitochondrial images (Figure 3B) do not accord with the lipid images (Figure 3E). Because the GFP images were acquired just before Raman measurement, it is unlikely that considerable intracellular reorganization of mitochondria occurred between the two measurements. Therefore, we confirm that mitochondria cannot account for the distribution pattern of lipids shown in Figure 3E. Second, lipid droplets provide a unique environment suitable for the storage of hydrophobic sterol esters, which are neither soluble in the aqueous cytosol nor present as typical lipid bilayer membranes (Czabany et al., 2007). The steroid part of the major class of sterol esters in yeast is ergosterol. As mentioned above, a recent Raman spectroscopic study on lipid droplet fractions isolated from the tetraploid W4 strain of yeast suggests that ergosterol is the prominent contributor to the 1602 cm^{-1} band (Chiu et al., 2012). Because the lipid band at 1301 cm^{-1} and the 1602 cm^{-1} band exhibit a virtually identical distribution at any measurement time, it is reasonable to link them to the same organelle, most likely lipid droplets.

At 25 and 31 hr, the distribution patterns of the Raman images associated with lipid droplets (Figures 3E and 3F) correlate very well with that of the protein image at 967 cm^{-1} (Figure 3D), both showing high intensities near the two ends of the cell. To examine this colocalization phenomenon quantitatively, we performed structural cross-correlation image analysis for the Raman images of ^{13}C-labeled proteins (Figure 3D) and lipids (Figure 3E). The correlation image analysis compares signal intensities of two images on a pixel-by-pixel basis, yielding the correlation coefficient C_{ij} at each pixel. C_{ij} is calculated as follows (Barzda et al., 2005; Segawa et al., 2012):

$$C_{ij} = \frac{(a_{ij}/a_{\max})(b_{ij}/b_{\max})}{[(a_{ij}/a_{\max})(b_{ij}/b_{\max})]_{\max}}.$$

Here, a_{ij} and b_{ij} represent intensities at the (i,j)th pixel of the two images a and b. The correlation images so obtained show remarkably high correlation in the lipid-rich region only at 25 and 31 hr (Figure 3G). The correlation image at 37 hr reveals a less pronounced correlation between the 967 and 1301 cm^{-1} Raman images, with a more diffuse pattern compared with those at 25 and 31 hr. Another important point to note is that the colocalization phenomenon seems to be synchronized with the increase of lipid concentration (compare Figures 3E and 3G). In fact, the time when the correlation becomes evident coincides with the onset of the lipid increase. This finding provides a clue

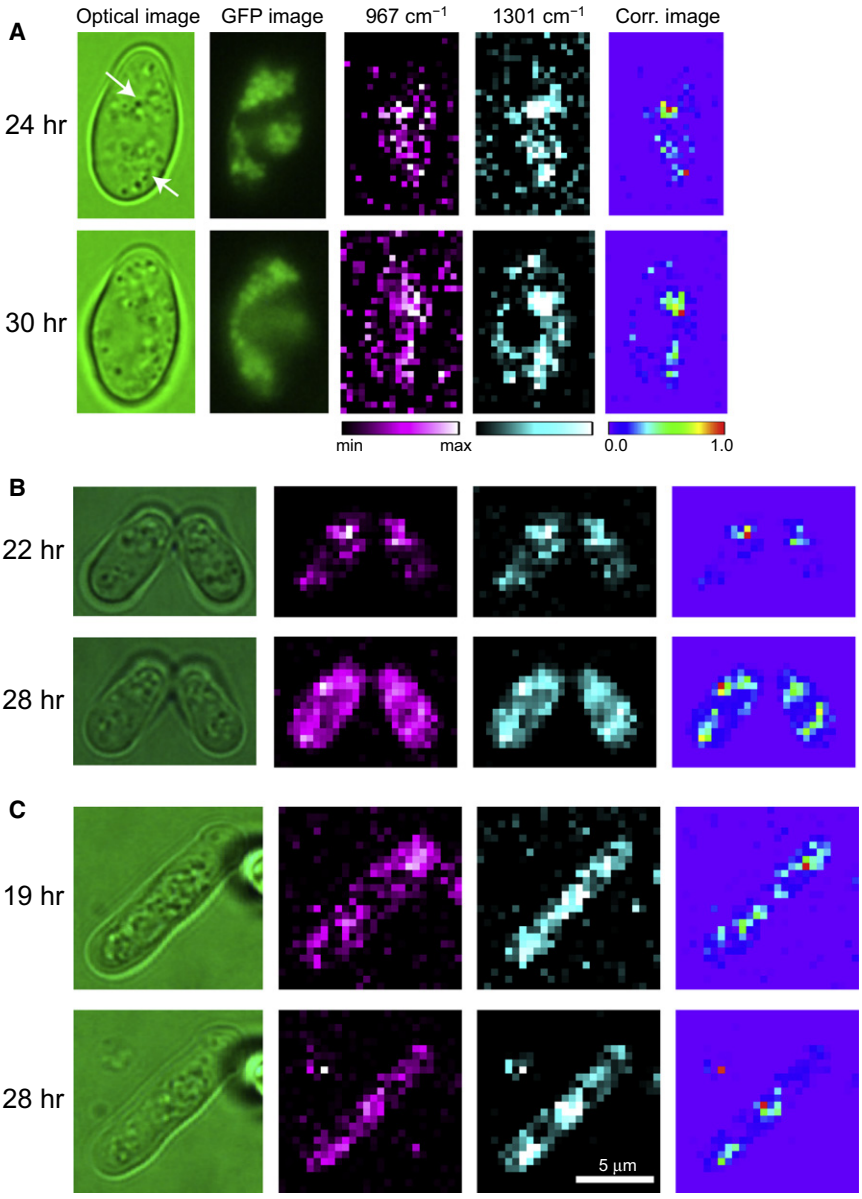

Figure 4. Time-Lapse Raman Imaging of Other Single Living *S. pombe* Cells Grown in ^{13}C-Glucose-Containing Medium

(A) The same GFP-labeled strain as in Figure 3. From left to right, the optical image, GFP image, Raman images at 967 and 1301 cm^{-1}, and their correlation image are shown. Arrows indicate the regions where many lipid droplets are found.

(B) A different wild-type strain (PR110) taken from early-log phase.

(C) Yet another wild-type strain (BCRC21605) taken from mid-log phase. The scale bar measures 5 μm and also applies to the other images.

to interpret the colocalization behavior from a physiological viewpoint of the *S. pombe* cell, as discussed below.

Last, we asked whether the colocalization phenomenon is accidental or specific to the *S. pombe* cell we chose. To address this question, we performed time-lapse Raman imaging on another three *S. pombe* cells. Raman images of the protein and lipid marker bands (967 and 1301 cm^{-1}, respectively) for the three cells at later stages after inoculation into ^{13}C-EMM are shown in Figure 4, together with their optical images, GFP images, and correlation images. The three cells differ in strain and/or growth phase from which the cell was chosen: namely, the same strain with GFP-labeled mitochondria as in Figure 3 (Figure 4A), a different wild-type strain (PR110) at early-log phase (Figure 4B), and yet another wild-type strain (BCRC21605) at mid-log phase (Figure 4C). Although we were unable to acquire a statistically significant number of single-cell data, all the cells studied (n = 4) showed, to a greater or lesser extent, a similar tendency of colocalization of newly formed proteins and lipid droplets at similar time scales, irrespective of strain and growth phase.

The Colocalization Phenomenon Might Be Induced by Starvation

What biological implications does the colocalization phenomenon have? As indicated by the Raman images of the 967 cm^{-1} band in Figures 3D and 4, the sole carbon source in the medium (^{13}C-glucose) is almost exhausted by ~20 hr because of its incorporation in the cell, putting the yeast cell in starvation. It has been shown that, under conditions of nutrition deprivation, lipid droplets increase in the cell to store more triacylglycerols for energy (Singh et al., 2009). As a consequence, when the cell starts to starve, proteins involved in lipid formation might be urgently synthesized from the remaining ^{13}C-substrate inside the cell and recruited to the site of action (i.e., lipid droplets). This recruitment results in the localization of ^{13}C-substituted proteins to lipid droplets in the time frame of 20–30 hr. In a generally accepted view, lipid droplet-associated proteins reside not in the core composed of neutral lipids but on the surface composed of phospholipid monolayer or in the close vicinity of lipid droplets. We presume that this is also the case with the localized proteins that we observed, but our spatial resolution of ~500 nm is not high enough to experimentally determine their more precise locations.

Recent studies suggest that lipid droplets might also sequester some denatured proteins until they are handed over to the cellular degradation machinery or temporarily store proteins for later use (Cermelli et al., 2006; Hodges and Wu, 2010; Welte, 2007). Apparently, our findings do not favor this mechanism, illustrating that lipid droplets are indeed involved in a variety of dynamic intracellular processes. Although more comprehensive studies are needed, the present study has shed an experimental light on such multifaceted and perhaps

interrelated roles of lipid droplets in relation to intracellular proteins.

SIGNIFICANCE

We have shown, by using in vivo time-lapse Raman imaging coupled with stable-isotope (^{13}C) labeling, that proteins synthesized via anabolic incorporation of ^{13}C-glucose into a single *S. pombe* cell are localized to lipid droplets. Although protein localization to other organelles, such as the nucleus, mitochodria, and the endoplasmic reticulum, in the fission yeast *S. pombe* was previously revealed by using a combination of cloning and fluorescence microscopy (Matsuyama et al., 2006), the localization to lipid droplets so far has not been observed by any other experimental methods. Because the fission yeast is the fundamentally most important model organism, our results not only provide direct evidence for the colocalization phenomenon along with the previous work on *Drosophila* embryos (Cermelli et al., 2006), but also suggest that it might be conserved in many organisms. The colocalization phenomenon we observed seems to occur when the intracellular concentration of lipids in the form of droplets is increased (e.g., by starvation). The conventional biological approach excels in revealing the identity and characteristic function of individual proteins associated with lipid droplets, but it still remains challenging to study the proteome and other intracellular components at the same time. Such studies would require many different probes to be introduced to the target cell, very likely resulting in considerable perturbation of cell physiology. In contrast, at the cost of the specificity to individual proteins, Raman spectroscopy can look at the proteome simultaneously (all protein molecules containing phenylalanine residues in the present case) without the need for tagging them with dye molecules. Moreover, it offers both space and time specificity, which cannot be achieved by imaging mass spectrometry (McDonnell and Heeren, 2007), another promising tool for bioimaging. Together, stable isotope-labeled Raman imaging should be a powerful, complementary addition to the arsenal of lipid droplet biology.

EXPERIMENTAL PROCEDURES

Cell Culture

Three different wild-type *Schizosaccharomyces pombe* strains were used in this study. Cells of each strain were cultured in Edinburgh Minimal Medium (EMM), which contained potassium hydrogen phthalate (3 g l^{-1}), Na_2HPO_4 (2.2 g l^{-1}), NH_4Cl (5 g l^{-1}), D-glucose (20 g l^{-1}), salts, vitamins, and minerals. For isotope substitution experiments, ^{13}C-D-glucose (99%, Cambridge Isotope Laboratories) was used. Solid EMM was prepared by adding agar (20 g l^{-1}). When studying yeasts in early-log and mid-log phases, a single colony taken from a 3-day-old ^{12}C-EMM agar was inoculated into 5 ml of ^{12}C-EMM broth and was grown for 7 and 20 hr, respectively. For experiments with yeasts in stationary phase, a single colony in a 3-day-old ^{12}C-EMM agar was taken as it was and inoculated into 200 μl of ^{13}C-EMM broth. In both cases, cells were harvested, washed twice, and appropriately diluted with distilled water. Two microliters of the culture was then inoculated into 200 μl of ^{13}C-EMM broth and was transferred to a poly-D-lysine-coated glass bottom dish. After the sample was left for 30 min so that cells were immobilized, it was transferred to a laboratory-made humidity chamber mounted on a piezoelectric stage of our Raman microscope (Huang et al., 2012). The chamber helped to maintain humidity around the dish and prevented such a small amount of medium (200 μl) from drying during a long measurement up to 40 hr.

Confocal Raman Microscopy and Imaging

Raman microspectroscopic and imaging experiments were performed with a laboratory-designed confocal Raman microspectrometer, as described previously (Huang et al., 2011, 2012; Noothalapati Venkata et al., 2011). The 632.8 nm line of a He-Ne laser was used as the Raman excitation light. In space- and time-resolved Raman measurements (bulk experiments), 2.4 mW laser power and 60 s exposure time were employed to increase the signal-to-noise ratio (SNR). In imaging experiments, the laser power was set to 1 mW to reduce photodamage as much as possible. In addition, the exposure time at each position was shortened to either 1.5 or 2 s, depending on the cell type and measurement time. The resulting image acquisition time was typically 16–20 min, which determined the time resolution of our imaging experiments. To improve the SNR of Raman spectra recorded with such a short exposure time, data preprocessing was performed by a singular value decomposition of the data matrix (Huang et al., 2012; Uzunbajakava et al., 2003; van Manen et al., 2004). The sample housed in the chamber was translated in a raster manner by the piezoelectric stage with a 0.47 μm step in both X and Y directions so that the laser spot scanned across the selected cell. Spectral acquisition was synchronized with sample scanning by the computer program LabVIEW (National Instruments). Lateral (XY) resolution was 0.47 μm, which was effectively determined by the step used in imaging experiments rather than by the estimated optical resolution (0.3 μm). Axial (Z) resolution was 2.4 μm. Because the typical thickness of an *S. pombe* cell is ~2 μm, the effective focal volume contained the whole cell along the Z direction. All measurements were done at 24°C.

To construct a Raman image, the intensity of the Raman band of interest was first obtained by calculating the area intensity between the band contour and a baseline connecting the two ends of an interval chosen to include the whole band (Huang et al., 2012). Curve fitting was not used for this purpose because of the low SNR. The Raman intensities evaluated at each point were then combined to construct a Raman image. The same procedure was repeated for all measurement times.

ACKNOWLEDGMENTS

We thank Professors Hiro-o Hamaguchi (the University of Tokyo) and Makoto Kawamukai (Shimane University) for providing us with the yeast strains used in this work. S.S. was supported in part by the National Science Council of Taiwan (Grant NSC100-2113-M-009-009-MY2).

Received: June 14, 2012
Revised: July 30, 2012
Accepted: August 28, 2012
Published: November 21, 2012

REFERENCES

Barzda, V., Greenhalgh, C., Aus der Au, J., Elmore, S., van Beek, J.H., and Squier, J. (2005). Visualization of mitochondria in cardiomyocytes by simultaneous harmonic generation and fluorescence microscopy. Opt. Express *13*, 8263–8276.

Brasaemle, D.L. (2007). Thematic review series: adipocyte biology. The prilipin family of structural lipid droplet proteins: stabilization of lipid droplets and control of lipolysis. J. Lipid Res. *48*, 2547–2559.

Cermelli, S., Guo, Y., Gross, S.P., and Welte, M.A. (2006). The lipid-droplet proteome reveals that droplets are a protein-storage depot. Curr. Biol. *16*, 1783–1795.

Chiu, L.D., Hullin-Matsuda, F., Kobayashi, T., Torii, H., and Hamaguchi, H. (2012). On the origin of the 1602 cm-1 Raman band of yeasts: contribution of ergosterol. J. Biophotonics *5*, 724–728.

Czabany, T., Athenstaedt, K., and Daum, G. (2007). Synthesis, storage and degradation of neutral lipids in yeast. Biochim. Biophys. Acta *1771*, 299–309.

Digel, M., Ehehalt, R., and Füllekrug, J. (2010). Lipid droplets lighting up: insights from live microscopy. FEBS Lett. *584*, 2168–2175.

Evans, C.L., Potma, E.O., Puoris'haag, M., Côté, D., Lin, C.P., and Xie, X.S. (2005). Chemical imaging of tissue *in vivo* with video-rate coherent anti-Stokes Raman scattering microscopy. Proc. Natl. Acad. Sci. USA *102*, 16807–16812.

Freudiger, C.W., Min, W., Holtom, G.R., Xu, B., Dantus, M., and Xie, X.S. (2011). Highly specific label-free molecular imaging with spectrally tailored excitation: stimulated Raman scattering (STE-SRS) microscopy. Nat. Photonics *5*, 103–109. http://dx.doi.org/10.1038/nphoton.2010.294.

Fujimoto, T., and Ohsaki, Y. (2006). Cytoplasmic lipid droplets: rediscovery of an old structure as a unique platform. Ann. NY Acad. Sci. *1086*, 104–115.

Grillitsch, K., Connerth, M., Köfeler, H., Arrey, T.N., Rietschel, B., Wagner, B., Karas, M., and Daum, G. (2011). Lipid particles/droplets of the yeast *Saccharomyces cerevisiae* revisited: lipidome meets proteome. Biochim. Biophys. Acta *1811*, 1165–1176.

Haider, S., Wagner, M., Schmid, M.C., Sixt, B.S., Christian, J.G., Häcker, G., Pichler, P., Mechtler, K., Müller, A., Baranyi, C., et al. (2010). Raman microspectroscopy reveals long-term extracellular activity of *Chlamydiae*. Mol. Microbiol. *77*, 687–700.

Hellerer, T., Axäng, C., Brackmann, C., Hillertz, P., Pilon, M., and Enejder, A. (2007). Monitoring of lipid storage in *Caenorhabditis elegans* using coherent anti-Stokes Raman scattering (CARS) microscopy. Proc. Natl. Acad. Sci. USA *104*, 14658–14663.

Hodges, B.D.M., and Wu, C.C. (2010). Proteomic insights into an expanded cellular role for cytoplasmic lipid droplets. J. Lipid Res. *51*, 262–273.

Huang, C.-K., Hamaguchi, H.O., and Shigeto, S. (2011). *In vivo* multimode Raman imaging reveals concerted molecular composition and distribution changes during yeast cell cycle. Chem. Commun. (Camb.) *47*, 9423–9425.

Huang, C.-K., Ando, M., Hamaguchi, H.O., and Shigeto, S. (2012). Disentangling dynamic changes of multiple cellular components during the yeast cell cycle by *in vivo* multivariate Raman imaging. Anal. Chem. *84*, 5661–5668.

Huang, W.E., Stoecker, K., Griffiths, R., Newbold, L., Daims, H., Whiteley, A.S., and Wagner, M. (2007). Raman-FISH: combining stable-isotope Raman spectroscopy and fluorescence *in situ* hybridization for the single cell analysis of identity and function. Environ. Microbiol. *9*, 1878–1889.

Huang, Y.-S., Karashima, T., Yamamoto, M., and Hamaguchi, H.O. (2005). Molecular-level investigation of the structure, transformation, and bioactivity of single living fission yeast cells by time- and space-resolved Raman spectroscopy. Biochemistry *44*, 10009–10019.

Jehmlich, N., Schmidt, F., Taubert, M., Seifert, J., Bastida, F., von Bergen, M., Richnow, H.-H., and Vogt, C. (2010). Protein-based stable isotope probing. Nat. Protoc. *5*, 1957–1966.

Kano, H., and Hamaguchi, H.O. (2007). Supercontinuum dynamically visualizes a dividing single cell. Anal. Chem. *79*, 8967–8973.

Li, T.S., Chen, Z.G., Johnson, J.E., and Thomas, G.J., Jr. (1990). Structural studies of bean pod mottle virus, capsid, and RNA in crystal and solution states by laser Raman spectroscopy. Biochemistry *29*, 5018–5026.

Manefield, M., Whiteley, A.S., Griffiths, R.I., and Bailey, M.J. (2002). RNA stable isotope probing, a novel means of linking microbial community function to phylogeny. Appl. Environ. Microbiol. *68*, 5367–5373.

Martin, S., and Parton, R.G. (2006). Lipid droplets: a unified view of a dynamic organelle. Nat. Rev. Mol. Cell Biol. *7*, 373–378.

Matsuyama, A., Arai, R., Yashiroda, Y., Shirai, A., Kamata, A., Sekido, S., Kobayashi, Y., Hashimoto, A., Hamamoto, M., Hiraoka, Y., et al. (2006). ORFeome cloning and global analysis of protein localization in the fission yeast *Schizosaccharomyces pombe*. Nat. Biotechnol. *24*, 841–847.

Matthäus, C., Boydston-White, S., Miljković, M., Romeo, M., and Diem, M. (2006). Raman and infrared microspectral imaging of mitotic cells. Appl. Spectrosc. *60*, 1–8.

Matthäus, C., Kale, A., Chernenko, T., Torchilin, V., and Diem, M. (2008). New ways of imaging uptake and intracellular fate of liposomal drug carrier systems inside individual cells, based on Raman microscopy. Mol. Pharm. *5*, 287–293.

McDonnell, L.A., and Heeren, R.M.A. (2007). Imaging mass spectrometry. Mass Spectrom. Rev. *26*, 606–643.

Murphy, S., Martin, S., and Parton, R.G. (2009). Lipid droplet-organelle interactions: sharing the fats. Biochim. Biophys. Acta *1791*, 441–447.

Nan, X., Cheng, J.-X., and Xie, X.S. (2003). Vibrational imaging of lipid droplets in live fibroblast cells with coherent anti-Stokes Raman scattering microscopy. J. Lipid Res. *44*, 2202–2208.

Naumann, D. (2001). FT-infrared and FT-Raman spectroscopy in biomedical research. Appl. Spectrosc. Rev. *36*, 239–298. http://dx.doi.org/10.1081/ASR-100106157.

Noothalapati Venkata, H.N., Nomura, N., and Shigeto, S. (2011). Leucine pools in *Escherichia coli* biofilm discovered by Raman imaging. J. Raman Spectrosc. *42*, 1913–1915. http://dx.doi.org/10.1002/jrs.2952.

Onogi, C., Torii, H., and Hamaguchi, H. (2009). Raman spectra of isotope-substituted mitochondria of living budding yeast cells: possible origin of the "Raman Spectroscopic Signature of Life". Chem. Lett. *38*, 898–899. http://dx.doi.org/10.1246/cl.2009.898.

Pol, A., Martin, S., Fernandez, M.A., Ferguson, C., Carozzi, A., Luetterforst, R., Enrich, C., and Parton, R.G. (2004). Dynamic and regulated association of caveolin with lipid bodies: modulation of lipid body motility and function by a dominant negative mutant. Mol. Biol. Cell *15*, 99–110.

Radajewski, S., Ineson, P., Parekh, N.R., and Murrell, J.C. (2000). Stable-isotope probing as a tool in microbial ecology. Nature *403*, 646–649.

Rinia, H.A., Burger, K.N.J., Bonn, M., and Müller, M. (2008). Quantitative label-free imaging of lipid composition and packing of individual cellular lipid droplets using multiplex CARS microscopy. Biophys. J. *95*, 4908–4914.

Saar, B.G., Freudiger, C.W., Reichman, J., Stanley, C.M., Holtom, G.R., and Xie, X.S. (2010). Video-rate molecular imaging in vivo with stimulated Raman scattering. Science *330*, 1368–1370.

Segawa, H., Okuno, M., Kano, H., Leproux, P., Couderc, V., and Hamaguchi, H.O. (2012). Label-free tetra-modal molecular imaging of living cells with CARS, SHG, THG and TSFG (coherent anti-Stokes Raman scattering, second harmonic generation, third harmonic generation and third-order sum frequency generation). Opt. Express *20*, 9551–9557.

Siamwiza, M.N., Lord, R.C., Chen, M.C., Takamatsu, T., Harada, I., Matsuura, H., and Shimanouchi, T. (1975). Interpretation of the doublet at 850 and 830 cm^{-1} in the Raman spectra of tyrosyl residues in proteins and certain model compounds. Biochemistry *14*, 4870–4876.

Singh, R., Kaushik, S., Wang, Y., Xiang, Y., Novak, I., Komatsu, M., Tanaka, K., Cuervo, A.M., and Czaja, M.J. (2009). Autophagy regulates lipid metabolism. Nature *458*, 1131–1135.

Thiele, C., and Spandl, J. (2008). Cell biology of lipid droplets. Curr. Opin. Cell Biol. *20*, 378–385.

Uzunbajakava, N., Lenferink, A., Kraan, Y., Volokhina, E., Vrensen, G., Greve, J., and Otto, C. (2003). Nonresonant confocal Raman imaging of DNA and protein distribution in apoptotic cells. Biophys. J. *84*, 3968–3981.

van Manen, H.-J., Kraan, Y.M., Roos, D., and Otto, C. (2004). Intracellular chemical imaging of heme-containing enzymes involved in innate immunity using resonance Raman microscopy. J. Phys. Chem. B *108*, 18762–18771. http://dx.doi.org/10.1021/jp046955b.

van Manen, H.-J., Kraan, Y.M., Roos, D., and Otto, C. (2005). Single-cell Raman and fluorescence microscopy reveal the association of lipid bodies with phagosomes in leukocytes. Proc. Natl. Acad. Sci. USA *102*, 10159–10164.

van Manen, H.-J., Lenferink, A., and Otto, C. (2008). Noninvasive imaging of protein metabolic labeling in single human cells using stable isotopes and Raman microscopy. Anal. Chem. *80*, 9576–9582.

Vartiainen, E.M., Peiponen, K.-E., and Tsuboi, T. (1990). Analysis of coherent Raman spectra. JOSA B *7*, 722–725. http://dx.doi.org/10.1364/JOSAB.7.000722.

Walther, T.C., and Farese, R.V., Jr. (2009). The life of lipid droplets. Biochim. Biophys. Acta *1791*, 459–466.

Welte, M.A. (2007). Proteins under new management: lipid droplets deliver. Trends Cell Biol. *17*, 363–369.

Wu, H., Volponi, J.V., Oliver, A.E., Parikh, A.N., Simmons, B.A., and Singh, S. (2011). In vivo lipidomics using single-cell Raman spectroscopy. Proc. Natl. Acad. Sci. USA *108*, 3809–3814.

